

# Imaging current distribution in a topological insulator Bi<sub>2</sub>Se<sub>3</sub> in the presence of competing surface and bulk contributions to conductivity

**Amit Jash**

Indian Institute of Technology Kanpur

**Ankit Kumar**

Indian Institute of Technology Kanpur

**Sayantan Ghosh**

Indian Institute of Technology Kanpur

**A. Bharathi**

UGC DAE Consortium for Scientific Research

**S. Banerjee** (✉ [satyajit@iitk.ac.in](mailto:satyajit@iitk.ac.in))

Indian Institute of Technology Kanpur

---

## Research Article

**Keywords:** 2D, TI, Bi<sub>2</sub>Se<sub>3</sub>, three-dimensional topological, electron doping

**Posted Date:** January 19th, 2021

**DOI:** <https://doi.org/10.21203/rs.3.rs-144104/v1>

**License:**  This work is licensed under a Creative Commons Attribution 4.0 International License.

[Read Full License](#)

---

**Version of Record:** A version of this preprint was published at Scientific Reports on April 2nd, 2021. See the published version at <https://doi.org/10.1038/s41598-021-86706-0>.

1           **Imaging current distribution in a topological insulator Bi<sub>2</sub>Se<sub>3</sub> in the presence of**  
2           **competing surface and bulk contributions to conductivity**

3           Amit Jash<sup>1</sup>, Ankit Kumar<sup>1</sup>, Sayantan Ghosh<sup>1</sup>, A. Bharathi<sup>2</sup>, S. S. Banerjee<sup>1\*</sup>

4  
5           <sup>1</sup>Department of Physics, Indian Institute of Technology Kanpur, Kanpur 208016, Uttar Pradesh, India

6           <sup>2</sup>UGC-DAE Consortium for Scientific Research, Kalpakkam-603104, India

7           \*corresponding author email: satyajit@iitk.ac.in.

8  
9           **Abstract:**

10          Two-dimensional (2D) topological surface states in a three-dimensional topological insulator (TI)  
11          should produce uniform 2D surface current distribution. However, our transport current imaging studies  
12          on Bi<sub>2</sub>Se<sub>3</sub> thin film reveal non-uniform current sheet flow at 15 K with strong edge current flow. This  
13          is consistent with other imaging studies on thin films of Bi<sub>2</sub>Se<sub>3</sub>. In contrast to strong edge current flow  
14          in thin films, in single crystal of Bi<sub>2</sub>Se<sub>3</sub> at 15 K our current imaging studies show the presence of 3.6  
15          nm thick uniform 2D sheet current flow. Above 70 K, this uniform 2D sheet current sheet begins to  
16          disintegrate into a spatially non-uniform flow. The flow becomes patchy with regions having high and  
17          low current density. The area fraction of the patches with high current density rapidly decreases at  
18          temperatures above 70 K, with a temperature dependence of the form  $1/|T - 70|^{0.35}$ . The temperature  
19          scale of 70 K coincides with the onset of bulk conductivity in the crystal due to electron doping by  
20          selenium vacancy clusters in Bi<sub>2</sub>Se<sub>3</sub>. Thus our results show a temperature dependent competition  
21          between surface and bulk conductivity produces a temperature dependent variation in uniformity of  
22          current flow in the topological insulator.

23  
24          **Introduction:**

25          In recent times the new class of materials viz., topological insulators (TI), have been  
26          extensively investigated. The interest has been fuelled by some of the intriguing properties of  
27          TI's materials, for example, their peculiar band structure which is characterised by a unique  
28          topological invariant index [1,2]. They possess a topologically protected bulk gapped state with  
29          conducting edge or surface state [1,2,3,4,5,6]. Any lattice distortions are incapable of  
30          destroying the topologically protected nature of the band structure in these TI materials.  
31          Theoretically, the two-dimensional (2D) TI possess a bulk gapped state while the sample edges  
32          are conducting due to the topological surface state. In contrast, the three dimensional (3D) TI

1 materials possess topological surface [4,7,8,9,10,11,12,13,14,15] states which are like uniform  
2 2D conducting sheets enclosing a gapped bulk. Time-reversal symmetry (TRS) protects these  
3 high electrically conducting gapless surface states in TI's. The TI possesses spin momentum  
4 locked current carrying states with opposite spins propagating in opposite directions. This  
5 suppresses back-scattering of electrons from disorder sites [2]. A characteristic feature of TI  
6 materials is that non - magnetic disorder does not affect the electrical conduction via the edge  
7 or surface states. The conducting edge/surface states exhibit Dirac-like linear energy-  
8 momentum dispersion [2], chiral spin texture [5] and Landau level quantization [16]. Akin to  
9 Si of the semiconductor world, Bi<sub>2</sub>Se<sub>3</sub> is the representative material for 3D TI's. Interpretation  
10 of bulk electrical transport measurements in 3D TI like Bi<sub>2</sub>Se<sub>3</sub>, Bi<sub>2</sub>Te<sub>2</sub>Se materials suggested  
11 that as per expectation, at low temperature there most likely exists 2D surface states [10,11].  
12 Direct imaging of currents in the 3D TI, Bi<sub>2</sub>Se<sub>3</sub> thin film using scanning SQUID microscopy  
13 [17], atom-chip microscopy [18] and scanning photo voltage measurements [19,20, 21],  
14 however showed the presence of one dimensional (1D) wire like currents flow along the film  
15 edges rather than 2D sheet current flow.

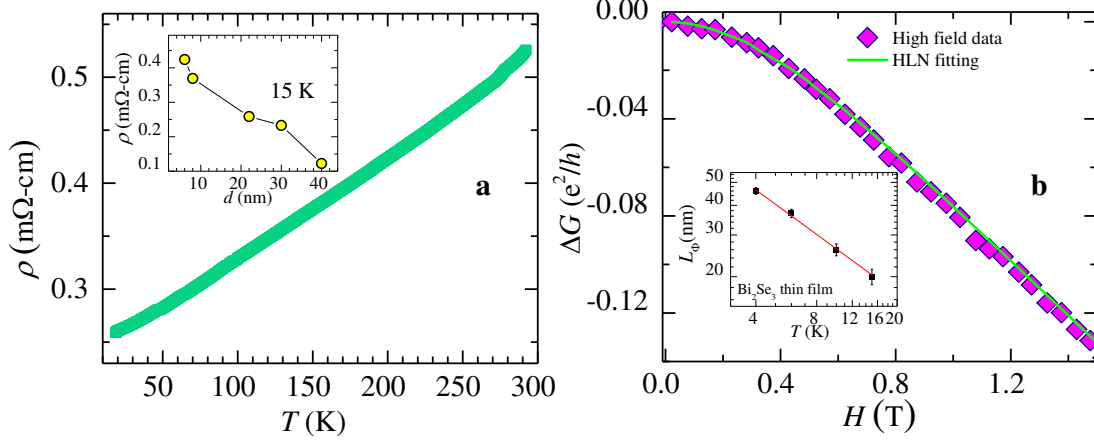
16 While most of the current imaging studies have been in high quality TI thin films, to the best  
17 of our knowledge there are none on TI single crystals. One may also note that very few imaging  
18 studies have explored the effect of non magnetic disorder on the nature of current distribution  
19 in these 3D TI materials. Typical non-magnetic defects found in 3D TI materials are, step edges  
20 of terraces on the surface of high - quality MBE grown films of TI [22] and vacancies in the  
21 atomic lattice of the TI's. It is known that the step edge defects locally produce a slight change  
22 in conductivity [22], however they do not produce any appreciable temperature dependent  
23 changes in the electrical conductivity of the TI. Although, defects like vacancy in TI  
24 significantly impacts the electrical conductivity of TI. Specifically, defects like selenium (Se)  
25 vacancies present in Bi<sub>2</sub>Se<sub>3</sub> electron dope the TI material bulk [23,24,25,26]. Thermally  
26 activated delocalization of these doped charges in the material bulk turns the insulating bulk of  
27 the TI into an electrically conducting region [23,28]. The disorder induced bulk conduction in  
28 TI bulk (which is insulating in an ideal TI) opens up an additional conduction channel which  
29 is in parallel to the topological high conduction edge or surface state channel already present  
30 in TI's. Recent bulk mutual inductance measurements in Bi<sub>2</sub>Se<sub>3</sub> [27,28] shows a predominance  
31 of topological surface state conductivity at low  $T$ , however beyond 70 K the bulk contribution  
32 grows and competes with surface conductivity. The studies show that above 70 K the bulk  
33 conductivity is of a thermally activated nature [27,28]. In view of the above issues in TI related

1 to transformation between surface and bulk contribution to conductivity, there have been few  
2 systematic imaging studies of current flow in 3D - TI over a wide temperature range. Motivated  
3 by the above issues, we image the current flow in a Bi<sub>2</sub>Se<sub>3</sub> from 15 K upto 290 K, using the  
4 high sensitivity magneto-optical self-field imaging technique. We use this current imaging  
5 technique to study the nature of surface and bulk current distribution TI thin film and single  
6 crystal. We also employ bulk electrical transport measurements to understand our results.  
7 Notably Bi<sub>2</sub>Se<sub>3</sub> thin film do not show uniform 2D sheet current flow, rather the flow is non -  
8 uniform sheet current. High current density flow is present along the film edges while a lower  
9 finite current density is present in the central regions of the film surface, away from the edges.  
10 Unlike the thin film, in Bi<sub>2</sub>Se<sub>3</sub> single crystal at low  $T$  we readily observe highly uniform  
11 topological 2D sheet current flow associated with 2D surface state in 3D TI. We determine the  
12 sheet current thickness to be  $\sim 3.6$  nm. With increasing temperature above 70 K, the uniform  
13 2D conducting sheet disintegrates into smaller patches with high and low current density ( $J$ )  
14 distribution. Such imaging of uniform 2D sheet current flow in 3D TI single crystal and  
15 tracking its evolution as a function of temperature, to the best of our knowledge hasn't been  
16 shown before. With decreasing  $T$ , the surface area fraction of the crystal with high  $J$  decreases  
17 rapidly above 70 K. The temperature dependence of the high  $J$  area fraction above 70 K follows  
18 the form,  $\frac{1}{|T - 70|^{0.35}}$ . Beyond 70 K, the observed features are related to the onset of  
19 thermally activated bulk conductivity in the TI due to activation of carriers doped in the bulk  
20 of the TI by Se vacancies.

## 21 **Results:**

### 22 **Transport measurement**

23 We grow epitaxial thin films of Bi<sub>2</sub>Se<sub>3</sub> of dimensions 2.1 mm  $\times$  2.1 mm  $\times$  30 nm on STO (111)  
24 substrates by RF sputtering (see method and section I of supplementary for characterization  
25 details). Note the thickness of our film (30 nm) is greater than the threshold thickness of 5 nm  
26 for Bi<sub>2</sub>Se<sub>3</sub>, below which the top and bottom topological surface states hybridize, producing a  
27 trivial insulator [29]. The Fig. 1a shows a metallic behaviour of bulk resistivity ( $\rho$ ) of the film  
28 measured as a function of increasing temperature ( $T$ ). The unavoidable presence of intrinsic  
29 defects, like Se vacancies which electron dope the Bi<sub>2</sub>Se<sub>3</sub> film [23,27] lead to metallic  
30 conductivity in Bi<sub>2</sub>Se<sub>3</sub>. Inset of Fig. 1a shows a rapid decrease of  $\rho$  because with increasing  
31 film thickness ( $d$ ). As Se vacancies concentration increases with increasing  $d$ , the doped charge  
32 (electron) concentration in the film also increases, resulting in a decrease in the  $\rho$ .



1

2 **Figure 1. Magneto-transport properties of Bi<sub>2</sub>Se<sub>3</sub> thin film.** (a) Shows the temperature dependence of the  
 3 resistivity of Bi<sub>2</sub>Se<sub>3</sub> thin film. Inset figure shows the thickness dependence of resistivity at 15 K. (b) Figure shows  
 4 the magneto-conductance in units of ( $e^2/h$ ), at 15 K. Green solid line shows fitting of the data to HLN equation  
 5 (see text for details). Inset figure shows the behaviour of the electron phase coherence length,  $L_\phi$ , as function of  
 6  $T$  on a log-log scale. The red line shows the linear behaviour (see text for details).

7

8 In zero applied magnetic field ( $H$ ), spin momentum locking of Dirac electrons in the  
 9 topological conducting surface state results in reduced back-scattering from disorder sites and  
 10 weak anti-localization (WAL) effect. In TI's at the special Dirac point in the energy -  
 11 momentum dispersion spectrum of the surface states, the momentum states ( $+k$  and  $-k$ ) are  
 12 doubly degenerate. Application of  $H$  lifts this degeneracy. At  $H = 0$  the conducting surface  
 13 states in TI have Berry phase ( $\phi$ ) =  $\pi$ . Breaking the time reversal symmetry (TRS) with  $H \neq$   
 14 0 results in a decreasing  $\phi$  with increasing  $H$ , and hence the conductance of the TI also  
 15 decreases, i.e.,  $\Delta G (H \neq 0) = G(H) - G(0) < 0$ . A combination of WAL along with TRSB effect  
 16 gives rise to an inverted cusp feature in  $\Delta G(H)$  for a TI. Figure 1b shows one half of the inverted  
 17 cusp in  $\Delta G(H)$  for our Bi<sub>2</sub>Se<sub>3</sub> film, for  $H > 0$ . Figure 1b shows  $\Delta G (H, 15 \text{ K})$  data, best fits the

18 Hikami, Larkin and Nagaoka (HLN) model [30], viz.,  $\Delta G = -\alpha \frac{e^2}{2\pi^2 h} \left[ \ln \left( \frac{B_\phi}{H} \right) - \psi \left( \frac{1}{2} + \frac{B_\phi}{H} \right) \right]$

19 , where  $\psi$  is digamma function,  $e$  is electronic charge,  $\alpha = 0.89 (\pm 0.02)$  and  $B_\phi = 0.4 \pm 0.01 \text{ T}$   
 20 are the best fit parameters at 15 K. The phase coherence length of the electron in the TI is,

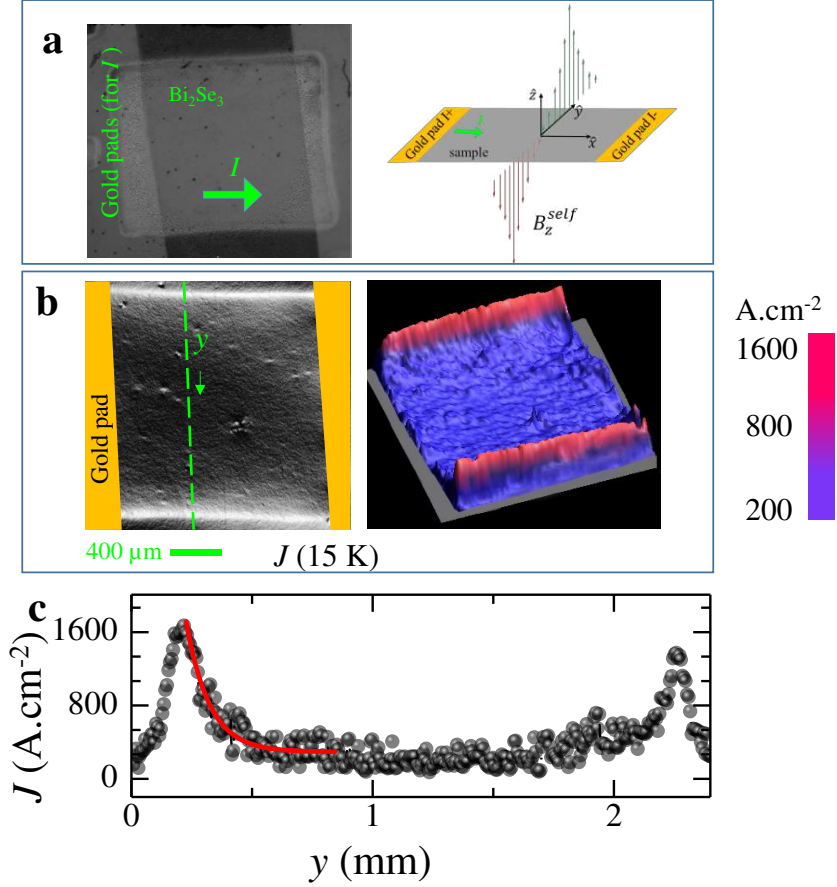
21  $L_\phi = \sqrt{\frac{h}{4eB_\phi}} = 48 (\pm 1.5) \text{ nm}$  at 4 K which decreases to  $L_\phi \sim 20 \text{ nm}$  at 15 K for the TI films

22 (see inset of Fig. 1b). The typical reported  $L_\phi$  values are, about 100 nm for Bi<sub>2</sub>Se<sub>3</sub> thin films

1 grown with MOCVD and about 65 nm for sputtered films [31,32]. The inset of Fig. 1b shows  
 2 a linear behaviour in a log - log plot of the phase coherence length  $L_\phi$  versus  $T$ , viz.,  $L_\phi \propto T^{-\lambda}$   
 3 , where  $\lambda = 0.62 \pm 0.02$ . The value of  $\alpha$  is a measure of the effective number of conduction  
 4 channels in the TI with  $\alpha = 1/2$  for each conduction channel [30]. From the fit at 4 K we get  $\alpha$   
 5 close to 0.5, signifying conduction via Dirac electrons in the TI's surface. At 15 K,  $\alpha$  increases  
 6 towards 1 suggesting that additional conduction channels are present in the TI film.

### 7 **MOISF of Bi<sub>2</sub>Se<sub>3</sub> thin film**

8 We visualize current flow across the TI film using the self-field magneto-optical imaging  
 9 technique (MOISF) (see methods), which has been used to visualize current distribution in  
 10 superconductors [33,34,35]. Briefly, MOISF technique involves high sensitivity spatial  
 11 mapping of the average Faraday rotation at every location on the sample. The rotation angle  
 12 relates to the self-field distribution,  $B_z^{self}(x, y)$  (where  $(x, y)$  are the co-ordinates on the sample  
 13 plane and  $z$  is perpendicular to it) generated by the current ( $I$ ) sent across a sample  
 14 (crystal/film). Figure 2a illustrates the schematic of  $B_z^{self}(y)$  behaviour across the sample  
 15 produced by the current. In the schematic, the  $B_z^{self}(y)$  is shown along an imaginary line (along  
 16 the  $y$  axis) drawn across the sample surface when current flows along the  $\hat{x}$  direction. The  
 17 length of the red and green vertical arrows schematically represents the variation in negative  
 18 and positive  $B_z^{self}$  values along  $y$ , respectively.



1

2 **Figure. 2. Edge current of thin film.** (a) Figure shows an optical image of Bi<sub>2</sub>Se<sub>3</sub> film showing the Cr/Au  
3 electrical pads sputtered on the film surface. Adjoining image is a schematic representation of the behaviour of  
4 the  $z$ -component of the self-field distribution. (b) Shows as gray-scale images and 3D map of the  $J(x, y)$   
5 distribution across the sample surface at 15 K. (c) The figure shows the  $J(y)$  profiles (measured along the dashed  
6 green line in Fig. b) at 15 K. The red solid line is a fit to the data using  $J = J_0 \exp(-\frac{y-y_0}{\delta}) + J_b$ , where  $J_0 = 1.6 \times 10^3$   
7 A/cm<sup>2</sup>,  $J_b = 260$  A/cm<sup>2</sup>,  $y_0 = 0.22$  mm and  $\delta = 96.70$  μm.

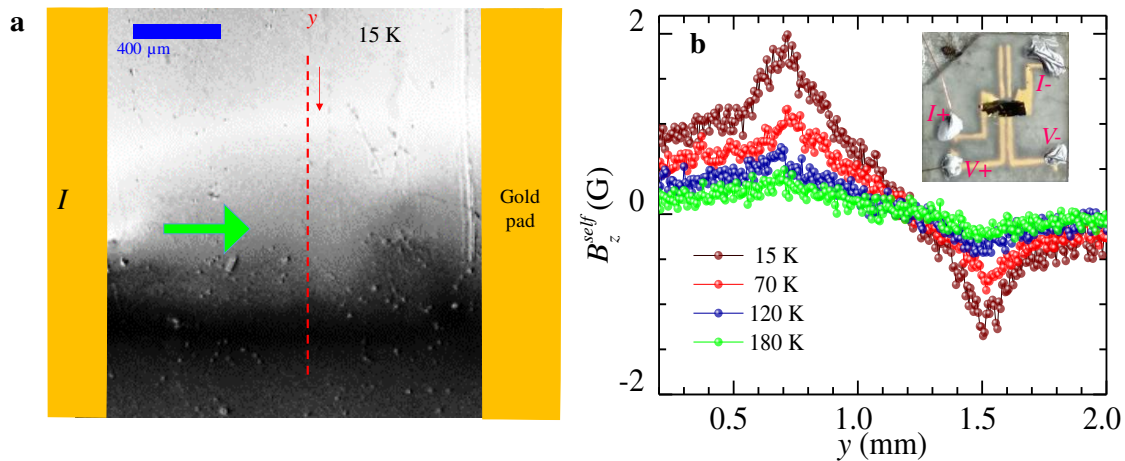
8 Using a numerical inversion scheme [36], from the measured  $B_z^{self}(x, y)$  we deduce the  $J_x(x, y)$   
9 and  $J_y(x, y)$  components of the current density  $J(x, y)$  distributed over the sample surface. The  
10 direction of  $J_x$  and  $J_y$  are along and perpendicular to the applied current direction, respectively.

11 In Fig. 2 we show only the magnitude of  $J(x, y) = \sqrt{J_x^2(x, y) + J_y^2(x, y)}$ . The overall direction  
12 of  $J$  is determined by the current sent into the TI sample. We calibrate the resultant  $J(x, y)$  map  
13 using the known current density in the Cr/Au contact pads. Figure 2a is an optical image of  
14 Bi<sub>2</sub>Se<sub>3</sub> thin film with Cr/Au contact pads. Figure 2b shows at 15 K, in a gray scale image the  $J$   
15 ( $x, y$ ) distribution with  $I = 35$  mA sent across the 30 nm thick Bi<sub>2</sub>Se<sub>3</sub> film. The strong bright  
16 contrast represents high  $J$  at the film edges. At first glance the images suggest that current flow

1 is through 1D wire like conducting edge states in a 3D TI. However, this is not possible as in  
 2 3D TI material such as ours has topological 2D high conducting surface states. Hence in 3D TI  
 3 material, one should observe 2D surface sheet current flow instead of 1D edge current flow  
 4 (which occurs only in 2D TI's). A closer examination of the  $J(y)$  profile in Fig. 2c (measured  
 5 along the green dashed line in Fig. 2b) shows existence of large  $J \sim 1600 \text{ A.cm}^{-2}$  at the film  
 6 edge which exponentially decays (see red fitted curve, in Fig. 2c) with a decay length  $\sim 96 \mu\text{m}$ .  
 7 This decay length is substantially larger than  $L_{\Phi} \sim 20 \text{ nm}$  (15 K) (see inset of Fig. 1b). Hence  
 8 the current at the edges isn't a pure one-dimensional wire like edge current rather it is  
 9 sufficiently broad. Note that the  $J$  in the central regions of the film away from the edges, isn't  
 10 zero, rather its  $\sim 200 \text{ A.cm}^{-2}$ . Thus, the edge  $J$  also doesn't decay down to zero over nm length  
 11 scales, as expected of purely one-dimensional edge current. Hence, the current flow in this 3D  
 12 TI film isn't via uniform 2D sheets rather it is via a non-uniform current sheet distributed over  
 13 the film surface. This non uniform current distribution on the film surface has large  $J$  peaks  
 14 near film edges with low but nonzero  $J$  in the central regions of the film. The 3D map of  $J(x,$   
 15  $y)$  in Fig. 2b confirms that the above feature isn't present at a few locations in the film but is  
 16 uniformly seen across the entire film, viz., a uniformly high  $J$  at film edges which exponentially  
 17 reduces to a smaller  $J$  in the film bulk.

### 18 $\text{MOI}_{\text{SF}}$ of $\text{Bi}_2\text{Se}_3$ single crystal

19



20

21 **Figure 3. Imaging of the self-field distribution on  $\text{Bi}_2\text{Se}_3$  single crystal.** (a) Figure shows self-field magneto  
 22 optical image representing  $z$ - component of self-field in the  $(x, y)$  plane, viz,  $B_z^{\text{self}}(x, y)$  measured at 15 K. The  
 23 green arrow represents the direction of the current ( $I$ ) sent into the sample from the pads. (b) Figure shows  $B_z^{\text{self}}(y)$

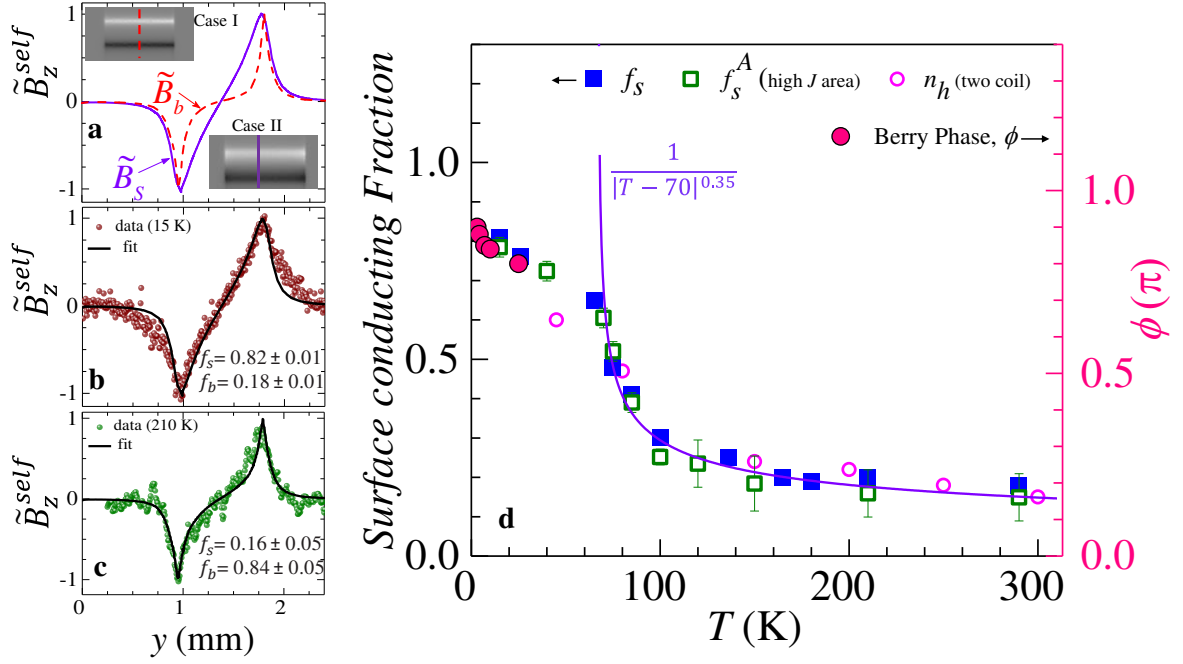
1 measured along the red dashed line in Fig. 3a at 15 K, 70 K, 120 K, and 180 K. Inset figure shows the optical  
 2 image of the Bi<sub>2</sub>Se<sub>3</sub> single crystal stuck on MgO substrate.

3 Here we investigate electrical transport in Bi<sub>2</sub>Se<sub>3</sub> single crystal. Supplementary section II,  
 4 shows Shubnikov de Has (SdH) oscillations (between 4 K until 25 K). The SdH oscillations  
 5 show the presence of high conducting surface states present in this crystal. In the section II of  
 6 supplementary, we show that the SdH is not due to the presence of a trivial two dimensional  
 7 electron gas in Bi<sub>2</sub>Se<sub>3</sub> but due to high conducting topological surface states located in the bulk  
 8 gap of the material. The SdH fit gives the value of the parameter  $\phi$ , viz., the calculated Berry  
 9 phase to be  $\sim \pi$ . This value is expected for high conducting topological Dirac electrons present  
 10 on the surface of TIs'. We image the current distribution in this single crystal of Bi<sub>2</sub>Se<sub>3</sub> using  
 11 MOISF technique. Figure 3a shows in gray scale the self-field  $B_z^{self}(x, y)$  distribution across a  
 12 Bi<sub>2</sub>Se<sub>3</sub> single crystal at 15 K with  $I = 35$  mA (note that if  $I$  were to distribute uniformly across  
 13 the crystal cross section then, it corresponds to a current density of 194 A/cm<sup>2</sup> for our crystal).  
 14 The white and black contrast in Fig. 3a corresponds to  $B_z^{self}(x, y)$  pointing either out of or into  
 15 the plane of the figure (see section III, shows a linear increase of  $B_z^{self}$  with  $I$ ). Figure 3b shows  
 16 the  $B_z^{self}(y)$  profile, measured at different  $T$  along the red dashed line in Fig. 3a. At low  $T$  (15  
 17 K) the peaks in  $B_z^{self}(x, y)$  are sharp, however as  $T$  increases the profile gets rounded off with a  
 18 decrease in  $B_z^{self}$  values. To understand the changes in the  $B_z^{self}(y)$  profiles with  $T$  in Fig. 3b,  
 19 we use COMSOL Multiphysics software to simulate field profile for 35 mA current sent  
 20 through a 1.6 mm  $\times$  0.9 mm  $\times$  0.02 mm conductor (dimension identical to our crystal) for two  
 21 different cases of current flow: Case I: Uniform cross-sectional current flow, viz., the  $B_z^{self}(y)$   
 22 generated by a current which is uniformly distributed across the sample cross - section (with  $J$   
 23 = 194 A/cm<sup>2</sup>) and Case II: Surface current flow, viz.,  $B_z^{self}(y)$  produced by only two 2D surface  
 24 current sheets (with  $J = 0.195$  A/cm) on the top and bottom surfaces of the crystal and zero  
 25 current in the sample bulk. Using finite current element analysis and the Biot-Savart's law, we  
 26 calculate the net  $B_z^{self}$  generated by the current distributions in cases I and II. Grey scale images  
 27 in the upper and lower panel of Fig. 4a show the simulated  $B_z^{self}(x, y)$  distribution for (case I)  
 28 and 2D surface sheet current (case II), respectively. Figure 4a compares the results for two  
 29 cases, using normalized  $\hat{B}_z^{self}(y) = B_z^{self}(y) / \max\{B_z^{self}\}$  for comparing the results. The  
 30  $\hat{B}_z^{self}(y)$  profiles for, the 2D surface current sheet (case II) and the bulk current (case I) are  
 31  $\hat{B}_s^{self}(y)$  and  $\hat{B}_b^{self}(y)$  respectively (see Fig. 4a). We convert the measured  $B_z^{self}(y)$  profiles

1 measured at 15 K and 210 K into  $\hat{B}_z^{elf}(y)$  (cf. Figs. 4b and 4c, respectively) and fit them with  
 2 Eq. (1),

$$3 \quad \hat{B}_z^{elf}(y, T) = f_s(T) \hat{B}_s^o(y) + f_b(T) \hat{B}_b^o(y) \quad (1)$$

4 Where  $f_s(T)$  and  $f_b(T)$  are the fraction of current flowing through the crystal 2D surfaces and  
 5 crystal bulk respectively, and they obey  $f_s(T) + f_b(T) = 1$ . Figure 4b shows the  $\hat{B}_z^{elf}(y)$  profile  
 6 at 15 K best fits Eq. (1) (black solid line) with  $f_s(T) = 0.82$  and  $f_b(T) = 0.18$ . Thus, at low  $T$ ,  
 7 the higher  $f_s$  value suggests a dominant 2D sheet current flow along the crystal surface with a  
 8 small fraction ( $f_b$ ) of current flowing through the crystal bulk. It is important to note that our  
 9 crystal thickness is well above the direct coupling limit (5 nm) of Bi<sub>2</sub>Se<sub>3</sub>. Hence, the observed  
 10 sheet current comprises topological Dirac surface electrons in Bi<sub>2</sub>Se<sub>3</sub> (recall the SdH  
 11 oscillations observed, see section II). Compared to 15 K, the fit to Fig. 4c at 210 K gives  $f_s(T)$   
 12 = 0.16,  $f_b(T) = 0.84$ , viz., at high  $T$  the fraction of current flowing through the crystal bulk  
 13 significantly increases compared to that at lower  $T$ . Figure 4d shows  $f_s(T)$  abruptly decreases  
 14 beyond 70 K, suggesting a transformation from surface to bulk dominated electrical transport.  
 15 Above, 200 K the contribution from surface sheet current flow has substantially reduced and  
 16 the contribution to conducting from the crystal bulk dominates. To validate these estimates,  
 17 Fig. 4d shows a close match between the values of high conducting surface fraction ( $n_h(T)$ )  
 18 determined using another technique, viz., two coil measurements [28] with the  $f_s(T)$  values.  
 19 We get the behaviour of the bulk contribution to electrical conduction of the TI, viz.,  $f_b(T)$ ,  
 20 using  $f_b(T) = 1 - f_s(T)$ , which shows an activated  $T$  dependence (see section IV of  
 21 supplementary). Earlier studies [27,28] show that thermal activation of the charges doped in  
 22 the bulk of Bi<sub>2</sub>Se<sub>3</sub> crystal because of Se vacancies begins from 70 K (see section V of  
 23 supplementary). This results in thermal activated behaviour of electrical conductivity above 70  
 24 K. Hence, the observed activated temperature dependence of  $f_b$  occurs due to the thermal  
 25 activation of doped charges in the bulk and its temperature dependence above 70 K is different  
 26 from the behaviour of  $f_s(T)$ .



1

2 **Figure. 4. Analysis of self-magnetic field profile and fraction of surface contribution of electrical**

3 **conductivity.** (a) Figure shows the simulated magnetic field profiles  $\tilde{B}_z^{self}(y)$  for bulk (case I) and surface (case

4 II) currents distributed in the crystal. Upper and lower panels show as grey scale images, the simulated self-field

5 distribution across the crystal, for the case I and II. Figures (b) and (c) show the behaviour of measured  $\tilde{B}_z^{self}(y)$

6 and the Eq. 1 fit to the measured  $\tilde{B}_z^{self}(y)$  data at 15 K, and 210 K, respectively. (d) Solid symbols show the

7 variation of surface contribution to conductivity using Eq. 1 fit (see text). The Berry phase ( $\phi/\pi$ ) versus

8 temperature (pink filled circles) calculated from the SdH oscillation observed on the magneto-resistance

9 measurements on the crystal (see section II of supplementary) is shown on the right vertical axis. The green square

10 symbol shows the area fraction of the high current density region ( $f_s^A$ ) as a function of temperature (see text for

11 details). Circle symbols represents the fraction of high conducting surface state ( $n_h$ ) measured as a function of

12 temperature, determined using the two-coil mutual inductance technique (reproduced from Fig. 5(a) of Ref. (28)).

13 The violet solid line is the functional form of  $1/|T-70|^{0.35 \pm 0.02}$ .

14 In Figs. 5a to 5d we show the  $J(x, y)$  distribution over the crystal surface at 15 K, 100 K, 210

15 K, and 290 K (determined from the  $B_z^{self}(x, y)$  profiles), as grey-scale images and coloured

16 maps, respectively. Consistent with the inference drawn from the above discussions at 15 K,

17 we see a uniform, high  $J$  ( $\sim 900$  A/cm<sup>2</sup>) two-dimensional (2D) current sheet on the crystal

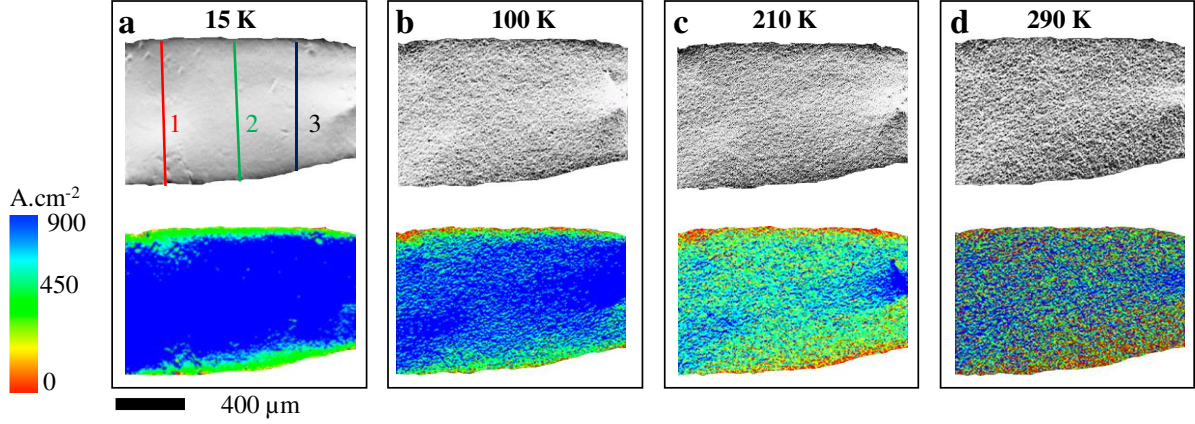
18 surface. This is in direct contrast to the non-uniform current distribution we had seen earlier

19 for the Bi<sub>2</sub>Se<sub>3</sub> thin film at 15 K. Our imaging in the single crystal confirms 2D high conducting

20 surface states associated with a 3D TI material present at low  $T$  in the crystal, a feature which

1 has not been imaged before. Note all prior imaging studies in thin films only saw one-  
 2 dimensional wire like edge current channels. With increasing  $T$ , the uniform, 2D high  $J$  ( $\equiv 770$   
 3  $\text{A/cm}^2$  -  $900 \text{ A/cm}^2$ ) surface sheet current in the crystal, disintegrates into low  $J$  (greenish and  
 4 light blue,  $J \leq 450 \text{ A/cm}^2$ ) and high  $J$  (dark blue) regions (Figs. 5b-5d). The onset of this  
 5 inhomogeneous  $J$  distribution in the current images sets in from 70 K onwards where there is  
 6 an increase in the distribution of current into the crystal bulk (viz., from where  $f_s(T)$  decreases  
 7 in Fig. 4d and  $f_b(T)$  increases (see section IV)). The smallest high  $J$  features at 210 K are  $\sim 10$   
 8  $\times 10 \mu\text{m}^2$ . These are above the spatial resolution of our magneto-optical setup of  $0.8 \mu\text{m}$ . Hence  
 9 we are not seeing any resolution limited features. We would like to mention that grainy feature  
 10 that develops in the current distribution at high  $T$  (see Fig.5 at 210 K) is also not due to noise  
 11 in the captured images. Had the graininess been an experimental artefact due to noise in the  
 12 images, then they should be present outside the sample as well as inside the sample. In the  
 13 supplementary information section VI, we explicitly show the absence of any of these grainy  
 14 features either in the raw or the coloured images outside the sample boundaries. We use images  
 15 like those in Fig. 5, to measure the area of the high  $J$  (dark blue regions  $\equiv 770 \text{ A/cm}^2$  -  $900$   
 16  $\text{A/cm}^2$ ) regions at different  $T$  and determine  $f_s^A = [\text{total area of high } J \text{ (dark blue regions )}$   
 17  $\text{regions}]/[\text{crystals top surface area}]$ . Figure 4d shows  $f_s^A(T)$  has an identical  $T$  dependence as  
 18 the behaviour of the topological high conducting surface states  $f_s(T)$  determined from analysis  
 19 of  $B_z^{self}$  profiles. A pure Dirac electron in 3D TI has a Berry phase ( $\phi$ ) =  $\pi$ . Figure 4d (pink  
 20 filled circles) shows that in the crystal at low  $T$  (below 25 K), the ( $\phi/\pi$ ) value (determined from  
 21 SdH fit, section II) is close to 1 and its  $T$  dependency is identical to that of  $f_s^A(T)$  and  $f_s(T)$   
 22 . The comparison in Fig. 4d confirms that at low  $T$  the fluid of topological Dirac electrons  
 23 uniformly covers the maximum surface area of the crystal. With the bulk conduction increasing  
 24 from 70 K, consequently the 2D conducting sheet disintegrates into patches. The smaller dark  
 25 blue patches which contain the high  $J$  ( $770 \text{ A/cm}^2$  -  $900 \text{ A/cm}^2$ ) topological Dirac surface  
 26 electron fluid are surrounded by normal electron fluid from bulk state which has a lower  $J$  ( $\leq$   
 27  $450 \text{ A/cm}^2$ ). With increasing  $T$  above 70 K, the normal electron contribution arises in the TI  
 28 because of an increasing bulk contribution to the electrical conduction. From the  $J(x, y)$   
 29 distribution at 15 K (Fig. 5a) we estimate the average effective thickness ( $d_{eff}$ ) of the topological  
 30 conducting surface current sheet. We determine a quantity  $K$  by integrating  $J$  along each of the  
 31 solid lines marked 1, 2, and, 3 in Fig. 5a, viz.,  $K_{1,2,3} = \int_{1,2,3} J \cdot dl$ , where  $dl$  is the length element

1 along the line. Using,  $K \cdot (2d_{eff}) \sim I$  for each of the lines (1, 2, 3), where  $I = 35$  mA (factor two  
 2 is for currents distributed along the top and bottom surface sheets in the TI) we get an average  
 3  $d_{eff} \sim 3.6 \pm 1.0$  nm. This value we have determined for the single crystal is close to the  
 4 approximately 3 nm thickness of the topological surface state found in thin films of TI [37,38].



5

6 **Figure. 5. The evolution of  $J(x, y)$  distributions.** Shows the  $J(x, y)$  distributions in grayscale and RGB scale  
 7 inside the sample at (a) 15 K, (b) 100 K, (c) 210 K and (d) 290 K (see text for details).

8 **Discussion:**

9 In real 3D TI material like  $\text{Bi}_2\text{Se}_3$  at low  $T$  the topological Dirac electron present on the surface  
 10 of the material dominates in conduction. However, as the TI material gets electron doped via  
 11 the Se vacancies, hence a conventional fluid of electrons appears in the material bulk at finite  
 12 temperatures. Figure 4d show the surface fraction decreases with temperature but it has an  
 13 abrupt break in curvature of the  $f_s^A(T)$  close to 70 K. Figure 4d shows that above 70 K,

14 
$$f_s^A(T) \propto \frac{1}{|T - 70|^{0.35 \pm 0.02}},$$
 suggesting an almost critical like behaviour at 70 K. Recall our

15 discussion of Fig. 5 had shown that near 70 K, coinciding with the onset of current distributing  
 16 through the crystal bulk, the current flow transforms from a uniform 2D sheet current flow into  
 17 patches of high and low  $J$ . Earlier studies [12,25] show that the thermal activation energy of  
 18 the charges doped in the bulk of  $\text{Bi}_2\text{Se}_3$  crystal because of Se vacancies, is around 70 K [ see  
 19 section V, refs. 27,28]. A recent room temperature STM study showed that nanoscale voids  
 20 and defects in TI produce local variations in the topological surface state [39]. Our  
 21 measurements show distinct features, viz., while ref. [39] found local changes at the nanometer  
 22 level which are temperature independent, we see high and low  $J$  macroscopic sized patches  
 23 develop only after  $T$  crosses 70 K. At low  $T$  there is the topological Dirac electron fluid phase  
 24 on the crystal surface which gives rise to uniform high  $J$ , 2D sheet current flow. Above 70 K a

1 significant concentration of Se vacancy doped conventional electron fluid appears in the  
2 material bulk and we see the inhomogeneity in  $J$  distribution with patches of high  $J$  ( $770 \text{ A/cm}^2$   
3 -  $900 \text{ A/cm}^2$ ) region embedded in low bulk current density ( $\leq 450 \text{ A/cm}^2$ ). We expect that,  
4 these two fluids have very different average energies as they occupy different bands in the  
5 material. With increasing  $T$ , especially above 70 K, the two fluids interact strongly. While we  
6 do not yet understand the nature of the complex interactions.

7 In summary, our study of  $\text{Bi}_2\text{Se}_3$  single crystal at low  $T$  shows 2D like uniform surface state  
8 with high  $J$ . With increasing  $T$  above 70 K, the 2D like surface state with uniform high  $J$  sheet  
9 breaks up into smaller regions with high and low  $J$  distribution. Thermally activated  
10 delocalization doped charges generated by Se vacancies in the 3D TI bulk triggers this  
11 transformation. Future studies need to explore the quantum equivalent of this transition in 3D-  
12 TI. Such studies we hope will have a deep impact on our fundamental understanding of the  
13 properties of 3D TI materials and their technological applications.

14

## 15 **Material and methods:**

### 16 **Material**

17 We study a single crystal of  $\text{Bi}_2\text{Se}_3$  prepared by slow cooling of stoichiometric melts of high  
18 purity Bismuth (Bi) and Selenium (Se) powders. The crystal has dimensions of  $1.9 \text{ mm} \times 0.9$   
19  $\text{mm} \times 0.02 \text{ mm}$ . We have already investigated crystals from the same batch earlier using  
20 electrical transport [24] and two-coil mutual inductance techniques [27,28]. Mechanical  
21 exfoliation gave freshly cleaved flat surface of the  $\text{Bi}_2\text{Se}_3$  crystal. The Cr (5 nm) /Au (50 nm)  
22 electrical contact pads are DC sputtered on to the crystal / film surface. The four-probe  
23 resistance  $\sim 10 \text{ m}\Omega$  (300 K). We grew epitaxial thin films of  $\text{Bi}_2\text{Se}_3$  of dimensions  $2.1 \text{ mm} \times$   
24  $2.1 \text{ mm} \times 30 \text{ nm}$  on STO (111) substrates by RF sputtering (see section I of supplementary for  
25 thin film characterization). The SdH oscillations observed in our single crystal (see section II  
26 confirms that electrical conduction is predominantly via the topological surface states for  $T <$   
27  $25 \text{ K}$ ).

### 28 **Magneto conductance measurement:**

29 We measured the magneto - conductance of our  $\text{Bi}_2\text{Se}_3$  thin film using four probe geometry.  
30 We carried out high magnetic field transport measurement (solid square symbols in Fig. 1b)  
31 between 22 mT up to 6 T in the Physical Property Measurement System (PPMS, Quantum

1 Design, USA). Remnant field of  $\sim 20$  mT in the superconducting magnet coils in the PPMS  
 2 prevented sensitive low field conductivity measurements below 20 mT. We used a home-built  
 3 copper coil electromagnet for low field transport measurements from 1 mT up to 20 mT to  
 4 avoid the remnant field issues. By comparing data from the two setups at higher field  
 5 measurements, we determined good data overlap collected from the two setups.

## 6 SFI method

7 In conventional magneto-optic imaging (MOI) technique the magneto-optical intensity of the  
 8 Faraday rotated light reflected from the sample is proportional to the local magnetic field  $B_z(x,$   
 9  $y)$  distribution across the sample when placed in an external magnetic field. In MOI<sub>SF</sub> the Andor  
 10 iXon (electron multiplied) EMCCD camera records the spatial distribution of Faraday rotation  
 11 at every pixel in a  $512 \times 512$ -pixel image of the sample. The spatial distribution of the Faraday  
 12 rotation is proportional to the local field distribution across the sample. In our case current ( $I$ )  
 13 sent through the sample generates the self-field (viz., the local magnetic field). In this technique  
 14 we capture differential images by taking the difference of magneto-optical images with a  
 15 positive current ( $I+$ ) and negative (opposite) current direction ( $I-$ ) flowing through the sample.  
 16 The MOI<sub>SF</sub> is an image which shows the distributions of the magneto-optical intensity,  $I_{SF}(x,$   
 17  $y)$ , which is proportional to self-field distributions  $B_z^{self}(x, y)$  so,  $MOI_{SF} =$

$$18 \frac{1}{M} \sum_{j=1}^M \left[ \frac{1}{N} \sum_{i=1}^N (MOI_i(I+) - MOI_i(I-)) \right]_j, \text{ where the } (x, y) \text{ is a co-ordinate of a pixel in the}$$

19 image. The MOI<sub>SF</sub> images represents the self-field,  $B_z^{self}(x, y)$  generated by current  $I$ . To  
 20 improve the signal-to-noise ratio,  $N$  nos. we capture the images with positive ( $I+$ ) and negative  
 21 currents ( $I-$ ) and take the difference  $M$  number of times (in our case  $N = M = 20$ ). Using a  
 22 numerical inversion scheme [36] we transform the  $B_z^{self}(x, y)$  map into the current map  $J(x, y)$ .

23

## 24 References:

- 
1. Moore, J. E. The Birth of Topological Insulators. *Nature* **464**, 194 (2010).
  2. Hasan, M. Z. & Kane, C. L. Colloquium: Topological insulators. *Rev. Mod. Phys.* **82**, 3045 (2010).
  3. Hsieh, D., Qian, D., Wray, L., Xia, Y., Hor, Y. S., Cava, R. J. & Hasan, M. Z. A topological Dirac insulator in a quantum spin Hall phase. *Nature* **452**, 970 (2008).
  4. Fu, L., Kane, C. L. & Mele, E. J. Topological Insulators in Three Dimensions. *Phys. Rev. Lett.* **98**, 106803 (2007).

- 
5. Hsieh, D. *et al.* Observation of Unconventional Quantum Spin Textures in Topological Insulators. *Science* **323**, 919 (2009).
  6. Zhao, L., Deng, H., Korzhovska, I., Chen, Z., Konczykowski, M., Hruban, A., Oganessian, V. & Krusin-Elbaum, L. Singular robust room-temperature spin response from topological Dirac fermions. *Nat. Mater.* **13**, 580 (2014).
  7. Xia, Y. *et al.* Observation of a large-gap topological-insulator class with a single Dirac cone on the surface. *Nat. Phys.* **5**, 398 (2009).
  8. Chen, Y. L. *et al.* Experimental Realization of a Three-Dimensional Topological Insulator Bi<sub>2</sub>Te<sub>3</sub>. *Science* **325**, 178 (2009).
  9. Pan, Z.-H., Fedorov, A. V., Gardner, D., Lee, Y. S., Chu, S. & Valla, T. Measurement of an Exceptionally Weak Electron-Phonon Coupling on the surface of the Topological Insulator Bi<sub>2</sub>Se<sub>3</sub> Using Angle-Resolved Photoemission Spectroscopy. *Phys. Rev. Lett.* **10**, 187001 (2012).
  10. Durand, C., Zhang, X. G., Hus, S. M., Ma, C., McGuire, M. A., Xu, Y. & Li, A. P. Differentiation of surface and bulk conductivities in topological insulators via four-probe spectroscopy. *Nano letters*, **16**, 2213 (2016).
  11. Barreto, L., Kühnemund, L., Edler, F., Tegenkamp, C., Mi, J., Bremholm, M. & Hofmann, P. Surface-dominated transport on a bulk topological insulator. *Nano letters*, **14**, 3755 (2014).
  12. Gao, B. F., Gehring, P., Burghard, M. & Kern, K. Gate controlled linear magnetoresistance in thin Bi<sub>2</sub>Se<sub>3</sub> sheets. *Appl. Phys. Lett.* **100**, 212402 (2012).
  13. Xu, Y., Miotkowski, I., Liu, C., Tian, J., Nam, H., Alidoust, N., Hu, J., Shih, C. K., Zahid Hasan, M. & Chen, Y. P. Observation of topological surface state quantum Hall effect in an intrinsic three-dimensional topological insulator. *Nat. Phys.* **10**, 956 (2014).
  14. Ning, W. *et al.* Robust surface state transport in thin bismuth nanoribbons. *Sci. Rep.* **4**, 7086 (2014).
  15. Checkelsky, J. G., Hor, Y. S., Cava, R. J., & Ong, N. P. Bulk Band Gap and Surface State Conduction Observed in Voltage-Tuned Crystals of the Topological Insulator Bi<sub>2</sub>Se<sub>3</sub>, *Phys. Rev. Lett.* **106**, 196801 (2011).
  16. Cheng, P., Song, C., Zhang, T., Zhang, Y., Wang, Y., Jia, J. F., Wang, J., Wang, Y., Zhu, B.F., Chen, X., Ma, X., He, K., Wang, L., Dai, X., Fang, Z., Xie, X., Qi, X.L., Liu, C.X., Zhang, S.C. & Xue, Q. K. Landau Quantization of Topological Surface States in Bi<sub>2</sub>Se<sub>3</sub>, *Phys. Rev. Lett.* **105**, 076801(2010).
  17. Wang, Y. H., Kirtley, J. R., Katmis, F., Jarillo-Herrero, P., Moodera, J. S. & Moler, K. A. Observation of chiral currents at the magnetic domain boundary of a topological insulator. *Science*, **349**, 6251 (2015).
  18. Dellabetta, B. Hughes, T. L. Gilbert, M. J. Lev, B. L. Imaging topologically protected transport with quantum degenerate gases. *Phys. Rev. B*, **85**, 205442. (2012).
  19. Liu, Y. Besbas, J. Wang, Y. He, P. Chen, M. Zhu, D. Wu, Y. Lee, J. M. Wang, L. Moon, J. Koirala, N., Oh, S. & Yang, H. Direct visualization of current-induced spin accumulation in topological insulators. *Nat. Commun.* **9**, 2492 (2018).
  20. Seifert, P., Vaklinova, P. K., Ganichev, S., Kern, K., Burghard, M. & Holleitner, A.W. Spin Hall photoconductance in a three-dimensional topological insulator at room temperature. *Nat. Commun.* **9**, 331(2018).
  21. McIver, J. W., Hsieh, D., Steinberg, H., Herrero, P. J. & Gedik, N. Control over topological insulator photocurrents with light polarization. *Nat. Nano. Technol.* **7**, 96 (2012).
  22. Macedo, R. J., Harrison, S. E., Dorofeeva, T. S., Harris, J. S. & Kiehl, R. A. Nanoscale Probing of Local Electrical Characteristics on MBE-Grown Bi<sub>2</sub>Te<sub>3</sub> Surfaces under Ambient Conditions. *Nano. Lett.* **15**, 4241 (2015).

- 
23. Benia, H. M., Lin, C., Kern, K. & Ast, C. R. Reactive Chemical Doping of the Bi<sub>2</sub>Se<sub>3</sub> Topological Insulator. *Phys. Rev. Lett.* **107**, 177602 (2011).
  24. Devidas, T. R. *et al.* Role of Se vacancies on Shubnikov-de Hass oscillations in Bi<sub>2</sub>Se<sub>3</sub>: A combined magneto-resistance and positron annihilation study. *EPL*, **108**, 67008 (2014).
  25. Butch, N. P., Kirshenbaum, P., Syers, K., Sushkov, A. B., Jenkins, G. S., Drew, H. D. & Paglione, J. Strong surface scattering in ultrahigh-mobility Bi<sub>2</sub>Se<sub>3</sub> topological insulator crystals. *Phys. Rev. B* **81**, 241301 (2010).
  26. Steinberg, H., Gardner, D. R., Lee, Y. S. & Herrero, P. J. Surface State Transport and Ambipolar Electric Field Effect in Bi<sub>2</sub>Se<sub>3</sub> Nanodevices. *Nano Lett.* **10**, 5032 (2010).
  27. Jash, A., Nath, K., Devidas, T. R., Bharathi, A. & Banerjee, S. S. Noncontact Mutual-Inductance-Based Measurement of an Inhomogeneous Topological Insulating State in Bi<sub>2</sub>Se<sub>3</sub> single crystals. *Phys. Rev. Applied.* **12**, 014056 (2019).
  28. Jash, A., Ghosh, S., Bharathi, A. & Banerjee, S. S. Coupling-decoupling of conducting surface states in thick Bi<sub>2</sub>Se<sub>3</sub> single crystals. *Phys. Rev. B* **101**, 165119 (2020).
  29. Neupane, M. *et al.* Observation of quantum-tunnelling-modulated spin texture in ultrathin topological insulator films. *Nat. commun.* **5**, 3841 (2014).
  30. Taskin, A. A., Sasaki, S., Segawa, K. & Ando, Y. Manifestation of topological protection in transport properties of epitaxial Bi<sub>2</sub>Se<sub>3</sub> thin films. *Phys. Rev. Lett.* **109**, 066803 (2012).
  31. Kumar, R., Brom, J. E., Redwing, J. M. & Hunte, F. Magnetotransport phenomena in Bi<sub>2</sub>Se<sub>3</sub> thin film topological insulators grown by hybrid physical chemical vapor deposition. *J. Appl. Phys.* **117**, 065302 (2015).
  32. Wang, W. J., Gao, K. H. & Li, Z. Q. Thickness-dependent transport channels in topological insulator Bi<sub>2</sub>Se<sub>3</sub> thin films grown by magnetron sputtering. *Sci. Rep.* **6**, 25291 (2016).
  33. Banerjee, S. S. *et al.* Vortex nanoliquid in high-temperature superconductors. *Phys. Rev. Lett.* **93**, 097002 (2004).
  34. Kumar, A., Jash, A., Tamegai, T., Banerjee, S. S. Imaging the effect of drive on the low-field vortex melting phenomenon in a Ba<sub>0.6</sub>K<sub>0.4</sub>Fe<sub>2</sub>As<sub>2</sub> single crystal. *Phys. Rev. B.* **101**, 184516 (2020).
  35. Tokunaga, M., Tokunaga, Y. & Tamegai, T. Imaging of the Percolative conduction Paths and Their breakdown in Phase-Separated (La<sub>1-y</sub>Pr<sub>y</sub>)<sub>0.7</sub>Ca<sub>0.3</sub>MnO<sub>3</sub> with  $y = 0.7$ . *Phys. Rev. Lett.* **93**, 037203 (2004).
  36. Wijngaarden, R. J., Spoelder, H. J. W., Surdeanu, R. & Griessen, R. Determination of two-dimensional current patterns in flat superconductors from magneto-optical measurements: An efficient inversion scheme. *Phys. Rev. B.* **54**, 6742 (1996).
  37. Wang, M. X. *et al.* The Coexistence of Superconductivity and Topological Order in the Bi<sub>2</sub>Se<sub>3</sub> thin films. *Science* **336**, 52 (2012).
  38. Wu, L., Brahlek, M., Aguilar, R. V., Stier, A. V., Morris, C. M., Lubashevsky, Y., Bilbro, L. S., Bansal, N., Oh, S. & Armitage, N. P. A sudden collapse in the transport lifetime across the topological phase transition in (Bi<sub>1-x</sub>In<sub>x</sub>)<sub>2</sub>Se<sub>3</sub>. *Nat. Phys.* **9**, 410 (2013).
  39. Lu<sup>†</sup>pke F. *et al.* Electrical resistance of individual defects at a topological insulator surface. *Nat. Commun.* **8**, 15704 (2017).

### Acknowledgement:

SSB thanks Professor Krishnendu Sengupta (IACS, Kolkata) for useful valuable discussions and inputs. SSB acknowledges funding support from DST (AMT-TSDP and Imprint-II

---

programs), IIT Kanpur and help of T. R. Devidas from IGCAR Kalpakam, India (present address: Hebrew University Jerusalem, Israel). SG acknowledges CSIR, INDIA for funding supports.

**Author contributions:** AJ did all the, measurements, growth of films, analysis and helped in writing the paper. AK and SG helped in the experiments and analysis as well as contributed to writing the paper. AB lab grew the single crystals and also did some of the bulk transport measurements on the crystals we report in the supplementary. SSB helped in conceiving and designing the experiments and the techniques, as well as guiding the analysis and interpreted the data and also wrote the paper.

**Competing interests:** The authors declare no competing interests.

# Figures

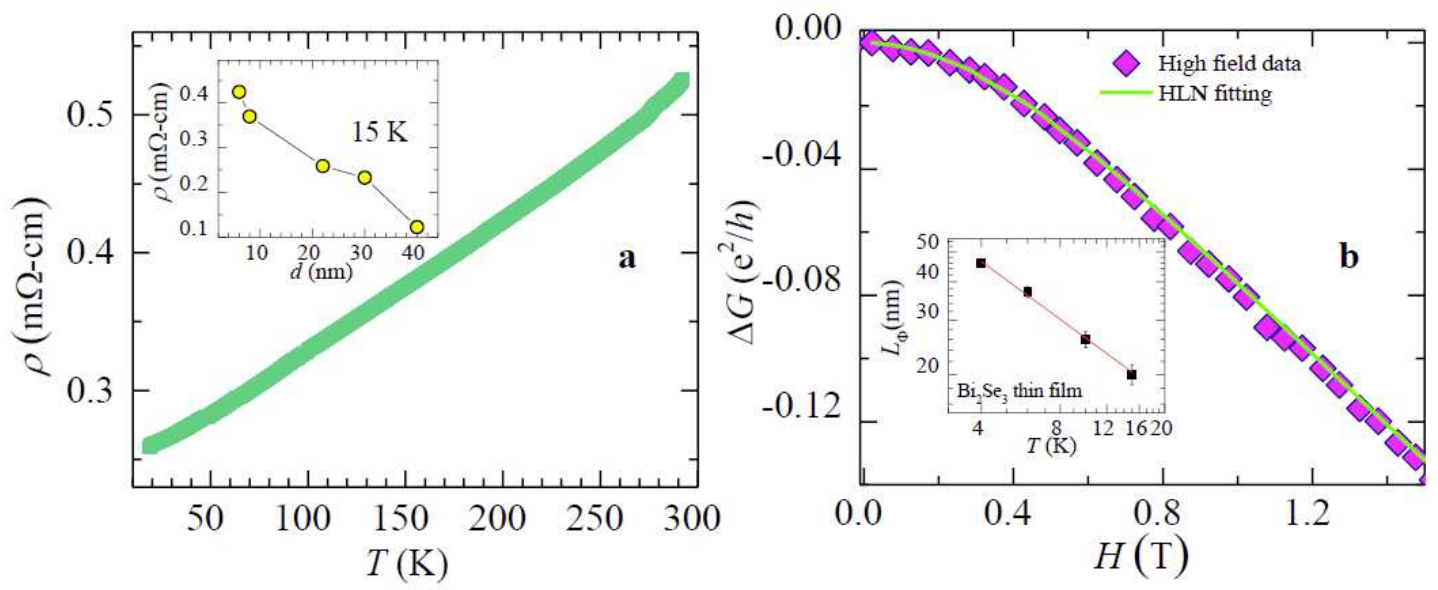


Figure 1

Magneto-transport properties of Bi<sub>2</sub>Se<sub>3</sub> thin film.

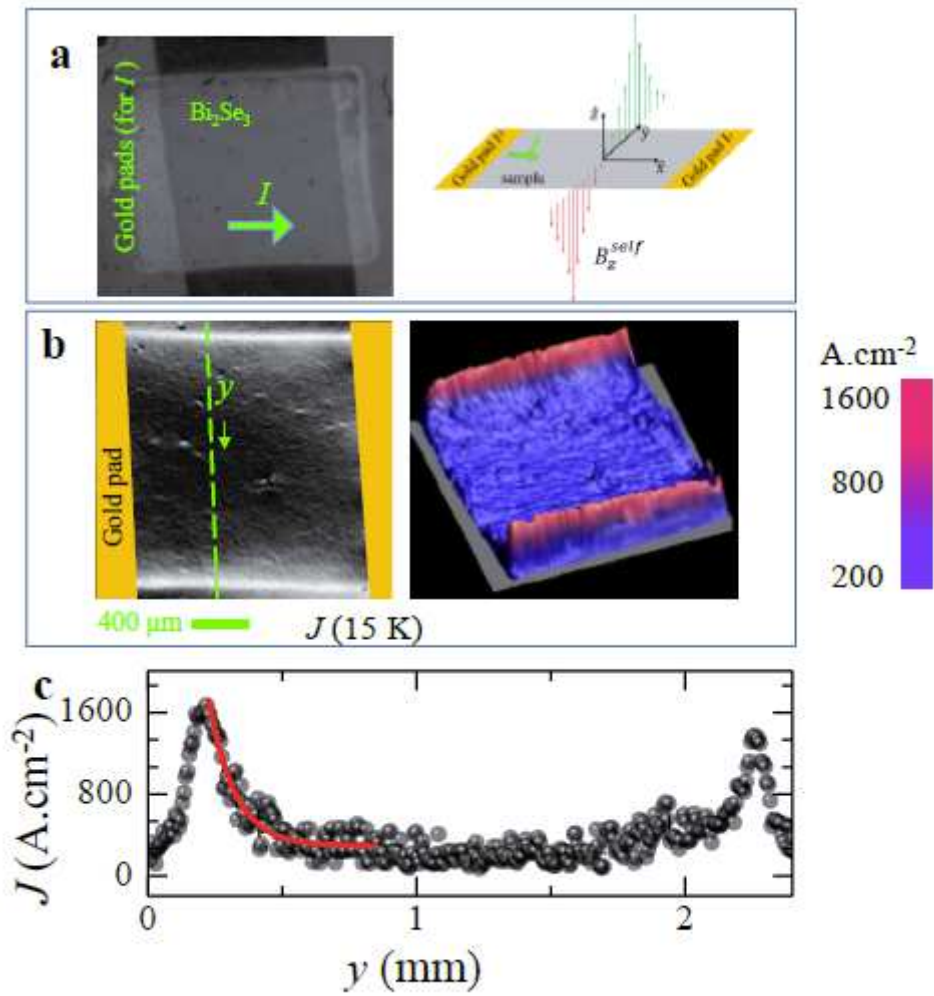


Figure 2

Edge current of thin film.

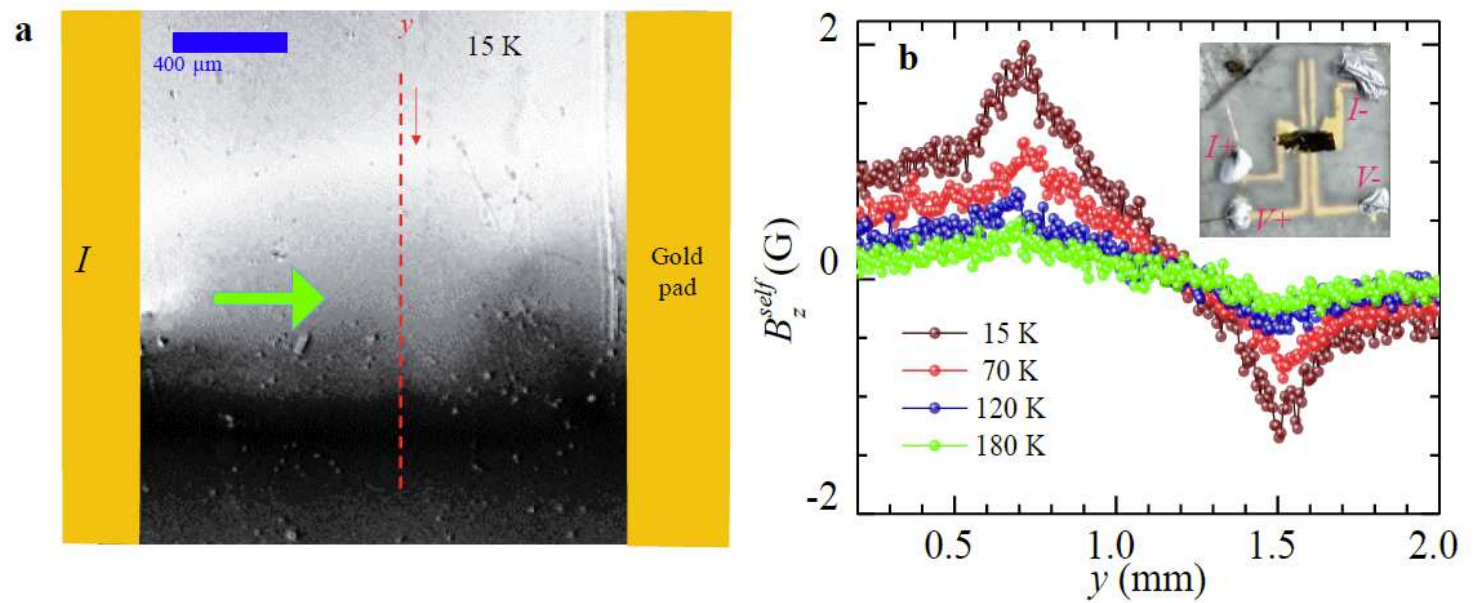


Figure 3

Imaging of the self-field distribution on Bi<sub>2</sub>Se<sub>3</sub> single crystal.

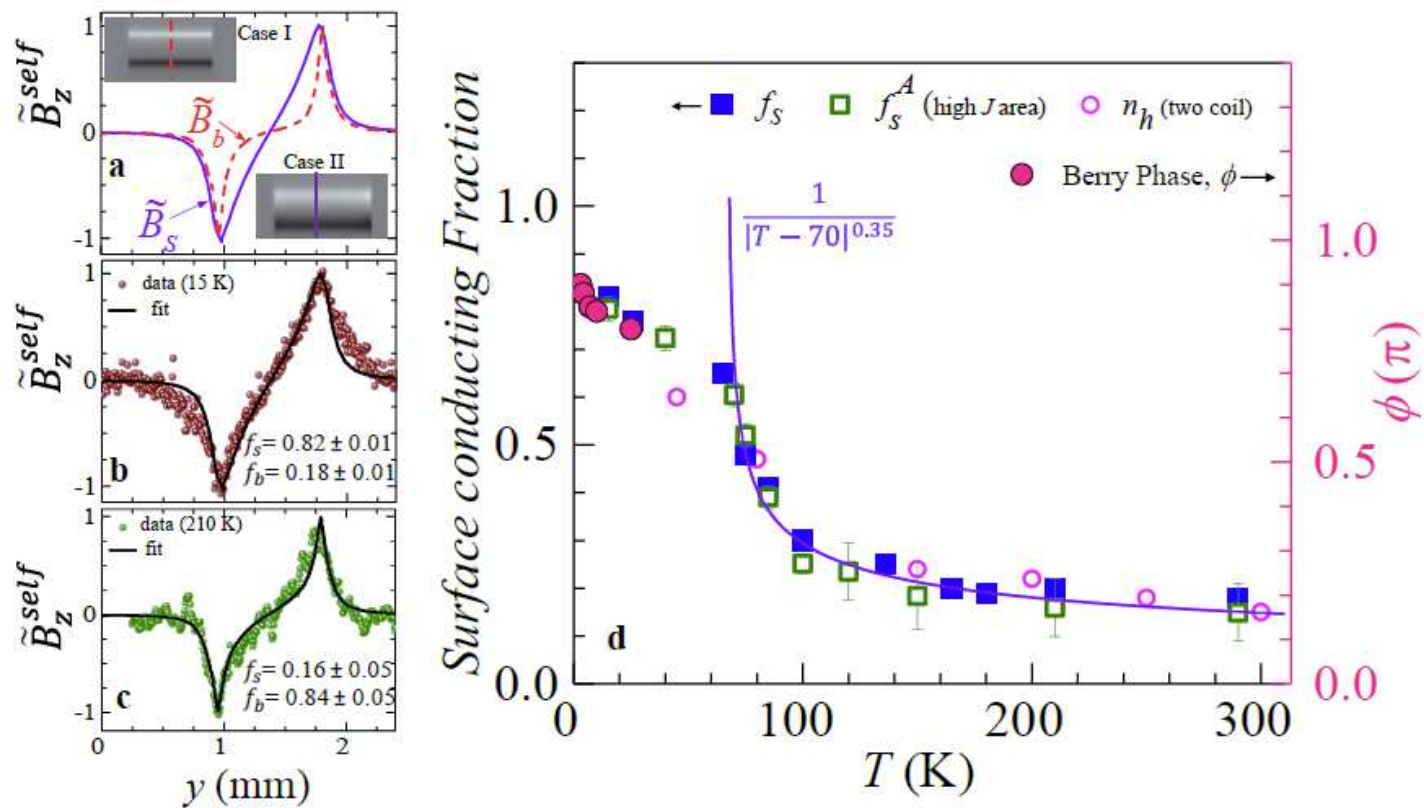


Figure 4

Analysis of self-magnetic field profile and fraction of surface contribution of electrical conductivity.

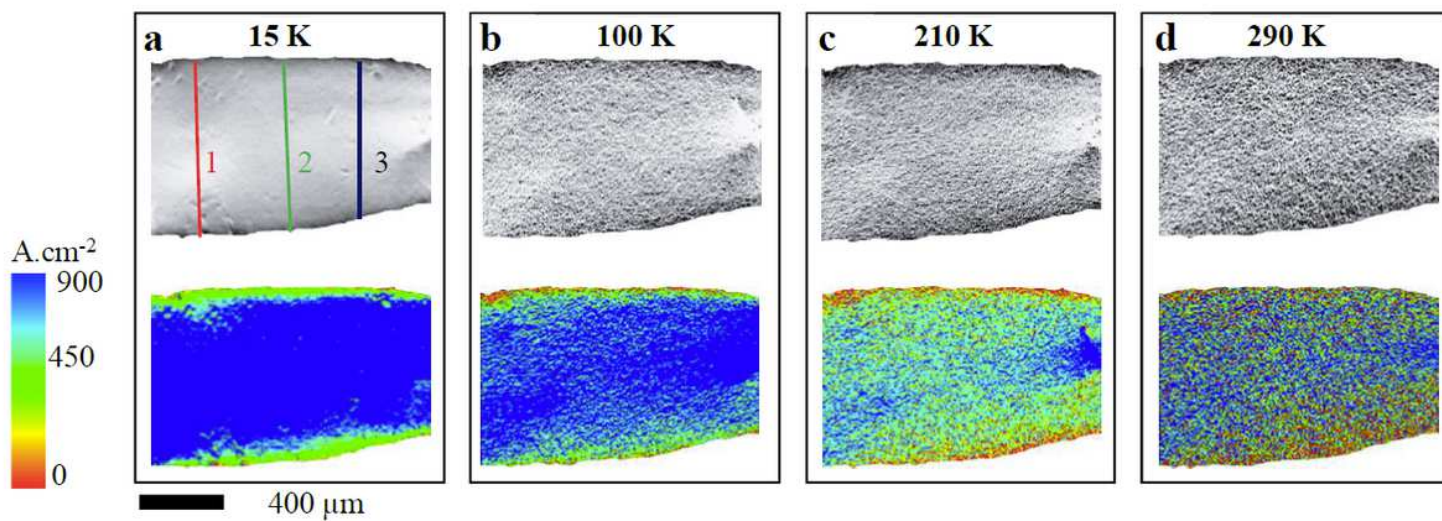


Figure 5

The evolution of  $J(x, y)$  distributions.

## Supplementary Files

This is a list of supplementary files associated with this preprint. Click to download.

- [supplementary12Dec.docx](#)